UNCLASSIFIED

AD ⎽406 157 ⎸⎽⎽

DEFENSE DOCUMENTATION CENTER

FOR

SCIENTIFIC AND TECHNICAL INFORMATION

CAMERON STATION, ALEXANDRIA, VIRGINIA

UNCLASSIFIED

THE STRUCTURE OF FREE

AND CONFINED TURBULENT VORTICES

By

JOE FLOYD THOMPSON, JR.

Research Note No. 44   May, 1963

TABLE OF CONTENTS

LIST OF FIGURES

LIST OF SYMBOLS

R, θ, Z cylindrical polar coordinates: Z axis is the axis of symmetry of the vortex.

v tangential velocity

u radial velocity

w axial velocity

W axial velocity at $R = 0$

W_∞ axial velocity at large R in wing-tip vortex

p static pressure

P_∞ static pressure at $R = \infty$

R radius of boundary layer

Γ circulation round the vortex at large R

K kinematic momentum

ρ density of the fluid

ϵ turbulent eddy viscosity

$\beta_{3\rho}$ turbulent wake function

T, F functions of R/R

D_c wing profile drag

c wing mean chord

k constant of porportionality

Subscripts:

ent denotes entrained flow

O denotes value at $R = 0$

max denotes maximum value

min denotes minimum value

$\widetilde{\widetilde{w}} = 0.5$ denotes value at $\widetilde{\widetilde{w}} = 0.5$

$\dfrac{W_\infty - w}{W_\infty - W} = 0.5$ denotes value at $\dfrac{W_\infty - w}{W_\infty - W} = 0.5$ in wing-tip vortex

N_{max} denotes value at $N = N_{max}$

μ_{max} denotes value at $\mu = \mu_{max}$

μ_{min} denotes value at $\mu = \mu_{min}$

$\mu = 0$ denotes value at $\mu = 0$

INTRODUCTION

From the bathtub drain to the airplane wing to the mushroom
cloud of a nuclear explosion the vortex occurs as a dominating fluid
flow feature. In fact, the vortex, or "eddy" as it is sometimes called
in reference to turbulence, is probably the most common and the most
important single fluid flow phenomenon; yet it remains one of the most
poorly understood. Vortices play an important part in the transition to
turbulence (Reference 1) and in meteorological storms (Reference 2).
Possible applications of the vortex are in heat exchangers (Reference 3),
gas separators and vortex reactors (Reference 4), (Reference 5), the
Ranque-Hilsch effect (Reference 6), advanced space propulsion (Reference
7), (Reference 8), and power generation systems (Reference 9), (Reference
10). Additional applications as well as an extensive bibliography of
recent work on vortices are given in reference 11.

Many of the older theoretical analyses of the vortex utilized highly
restrictive and, in many cases, unreal assumptions such as negligible
axial velocity or no variation of the tangential velocity in the axial direc-
tion. It is only through the use of such restrictive assumptions that exact
solutions of the full Navier-Stokes equations can be obtained for so com-
plex a flow. Recently, Long (Reference 12) obtained a numerical solution
of the laminar Navier-Stokes equations with boundary layer approximations
which is not too restrictive. In this solution, the axial velocity is of the
same order of magnitude as the tangential velocity for all radii. It is noted
by Long, however, that experimentally the axial velocity falls off faster
than the tangential velocity at large radii. Also recently, Lewellen (Ref-
erence 13) obtained a series solution of the laminar Navier-Stokes equations.
Newman (Reference 14), using boundary layer assumptions, linearized

and integrated the Navier-Stokes equations for viscous laminar vortical flow behind a wing tip. He then applied the laminar solution to a turbulent vortex by replacing the kinematic viscosity by an eddy viscosity. This assumption of an eddy viscosity which is a function of the circulation and kinematic momentum of the vortex but not of the radius or the axial coordinate has been used in most analyses of turbulent vortices. Newman (Reference 14) states that the eddy viscosity varies slightly in the radial direction and that this variation is about the same as in the turbulent jet. He also found variation of the eddy viscosity in the axial direction in the wing-tip vortex but attributed this variation to the incompleteness of the rolling up of the vortex rather than to actual variation of the turbulence level. Gasparek and Dosanjh (Reference 15) obtained experimental velocity measurements in a vortex behind an airfoil (NACA 0009) and compared these with Newman's theory.

In the present investigation, the turbulent entrainment analysis of the axi-symmetric free turbulent jet developed by Faris (Reference 16) is extended to describe the free turbulent vortex, and the resulting theory is compared with that of Newman (Reference 14) and the experimental data of Gasparek and Dosanjh (Reference 15).

The theory is then extended to describe the confined turbulent vortex and is compared with experimental measurements taken in a sink type vortex confined in a cylinder.

EXPERIMENTAL APPARATUS AND TECHNIQUES

Apparatus

The apparatus used to produce and study the confined turbulent vortex is shown in Figure 1. Figures 2 and 3 show close-ups of the 5.72 inches inside diameter plexiglas tube with the vortex core made visible by smoke.

The air entered tangentially at one end of the tube through a system of twelve one-inch high vanes set tangent to the tube and placed symmetrically around its circumference. The vanes were covered with a glass plate which permitted visual and photographic observation into the end of the tube.

A wooden plate with a 1.25 inches diameter hole in its center was located inside the tube 2.50 feet from the vanes. The plate fitted flush with the inside of the tube so that no airflow around its edges was possible. The air was pulled through the hole in the plate by a Joy Axivane fan connected to a Sola constant voltage transformer. A variac was used to vary the power to the fan and thus regulate the flow velocity.

The probe used in measuring the velocity profiles and its traversing mechanism are shown in Figure 4. The probe was made of progressively smaller diameter stainless steel tubing ending in a section 0.018 inch in diameter. Before the measurements, the probe tip was accurately adjusted to be exactly on the axis of the probe. The micrometer traversing mechanism was fitted with a calibrated angle adjustment device such that measurements could be taken at any angle to the axis of the tube.

Lines parallel to and in the same plane with the axis of the tube were scribed on each side of the tube to assist in orientation of the probe. A series of holes spaced 2 inches apart was drilled along one of the lines

to accommodate the probe. All holes except the one in use were covered
with tape. The tube was mounted in its supports so that the probe moved
in the plane containing the two lines and the tube axis. Final fine adjust-
ment of the probe into this plane was made with the two adjusting screws
at the base of the traversing mechanism. The aluminum block on the front
of the traversing mechanism was cut to conform exactly to the outside
diameter of the tube to insure that the probe axis was perpendicular to
the tube wall.

A strip of electrically conducting paint was painted on the inside of
the tube along the line opposite the holes. Batteries and a small bulb
were connected between the paint and the probe so that a complete circuit
was formed when the probe touched the paint. Thus, it was possible to
determine the exact micrometer setting at which the probe just touched
the wall without damage to the probe. The angle adjuster was zeroed
visually using the line scribed on the tube. Measurements were made
with a Kollsman helicopter airspeed indicator calibrated against a Betz
manometer.

Techniques

Because of the very large velocity gradient in the radial direction
(the tangential velocity increasing from zero at the centerline of the tube
to a maximum value in about one-fourth inch), it was impossible to measure
the static and total pressure at the same time as it conventional. Therefore,
at each setting of the micrometer, measurements were taken at two degrees
of angle intervals and at one degree intervals where necessary. The maxi-
mum pressure was then taken as the total pressure, and the minimum pressure,
which was located approximately 90 degrees from the maximum pressure,

was taken as the static pressure. The angle at which the total pressure occured was taken as the angle of the velocity vector.

The velocity was then calculated from the total and static pressure measurements, and its components in the tangential and axial directions were obtained from the angle of the velocity vector. About 45 measurements were taken between the wall and the centerline of the tube, at 0.20 inch intervals near the wall and at 0.020 inch intervals near the centerline.

The centerline was located by extrapolating the tangential velocity curve to zero. This accounted for the small irregularities in the thickness of the paint and in the tube.

Measurements were taken through five holes at the same variac setting, the five holes being 1.5, 5.5, 13.5, 21.5, and 26.5 inches from the plate. Also, measurements through the 13.5 inch hole were taken at a higher and a lower variac setting.

THEORETICAL DESCRIPTION OF THE FREE TURBULENT
SOURCE OR SINK TYPE VORTEX

Tangential Velocity

The tangential velocity of an inviscid, potential flow vortex is
given by

$$N = \frac{\Gamma}{2\pi n} ,$$

(1)

yielding infinite velocity at $n = 0$ (Figure 5). However, in a real
fluid the velocity discontinuity at $n = 0$ will be smoothed out by
the action of viscosity.

It was suggested by Cornish (Reference 17) that it might be possible
to obtain the viscous vortex tangential velocity profile by considering
the potential flow vortex velocity profile shown in Figure 5 to represent
two hypothetical adjacent jets in opposite directions. Following this
analogy, at $n = 0$ there exists a velocity discontinuity between the
two jets which must be smoothed out by mutual entrainment.

This turbulent entrainment process was analyzed by Faris (Reference
16) in his description of the axi-symmetric free turbulent jet. Using a
boundary layer approach, he found that the axial velocity in such a jet
can be given by

$$u = W(1 + \beta_{3D}) , \quad \frac{n}{R} \leq 1 ,$$

$$u = 0 , \quad \frac{n}{R} \geq 1$$

(2)

(see Figure 6). The function β_{3D} is a function of R/R , where $R(z)$ is the width of the jet, and is plotted in Figure 7. This function is very closely approximated by

$$\beta_{3D} \cong -\frac{1}{2}\left[1 + \cos \pi \left(1 - \frac{R}{R}\right)^2\right]$$ (3)

In direct analogy, the jet $\dfrac{\Gamma}{2\pi R}$ on the right side of the $R = 0$ line in Figure 5 entrains flow on the left side of the $R = 0$ line given by

$$N_{ent} = \frac{\Gamma}{2\pi R}\left(1 + \beta_{3D}\right),$$ (4)

where $R(z)$ now is the width of the zone of influence on each jet on the other.

Thus, as is shown in Figure 8, the entrainment velocity of each jet is opposite in direction to the primary velocity of the other jet so that the resultant velocity is obtained by subtracting the entrainment velocity of each jet from the primary velocity of the other. This resultant velocity profile is then taken as the viscous free turbulent vortex tangential velocity profile and is shown by the dotted curve in Figure 8.

Therefore, the tangential velocity of the free turbulent vortex is given by

$$N = \frac{\Gamma}{2\pi R} - \frac{\Gamma}{2\pi R}\left(1 + \beta_{3D}\right), \quad \frac{R}{R} \le 1,$$

or,

$$v = -\frac{\Gamma}{2\pi R} \frac{\beta_{3D}}{\left(\frac{r}{R}\right)} \quad , \quad \frac{r}{R} \leq 1. \tag{5}$$

As can be seen in Figure 8, $R(z)$ is the radius of the boundary layer within which the effects of viscosity alter the potential flow profile. Outside the boundary layer $\left(\frac{r}{R} \geq 1\right)$ the effects of viscosity are negligible, and the tangential velocity is given by the potential flow expression:

$$v = \frac{\Gamma}{2\pi r} \quad , \quad \frac{r}{R} \geq 1. \tag{6}$$

Pressure

According to the usual boundary layer approximations for vortex flow (Long, Reference 18) the centrifugal force and the pressure gradient force are the only important terms in the radial Navier-Stokes equation:

$$\frac{v^2}{r} = \frac{1}{\rho} \frac{\partial p}{\partial r} \tag{7}$$

Therefore, the pressure is given by

$$\frac{p}{\rho} = \int \frac{v^2}{r} dr + f(z) . \tag{8}$$

Substitution of $\mathcal{N}$ from (5) and (6) and application of the boundary condition at $\mathcal{R} = \infty : \mathcal{P} = \mathcal{P}_\infty$ yields (Appendix A)

$$\frac{P}{\rho} = \frac{P_\infty}{\rho} + \left(\frac{\Gamma}{2\pi R}\right)^2 \left[F\left(\frac{\mathcal{R}}{R}\right) - 5.79\right] , \quad \frac{\mathcal{R}}{R} \leq 1, \quad (9)$$

$$\frac{P}{\rho} = \frac{P_\infty}{\rho} - \frac{1}{2}\left(\frac{\Gamma}{2\pi \mathcal{R}}\right)^2 , \quad \frac{\mathcal{R}}{R} \geq 1. \quad (10)$$

The function $F\left(\frac{\mathcal{R}}{R}\right)$ is plotted in Figure 9.

Axial Velocity

In a real vortex the axial velocity is in general not negligible as is often assumed. It is thought that the same tangential velocity and pressure distribution may exist with various modes of the axial velocity depending on the kinematic momentum and boundary conditions. It will be assumed here, subject to subsequent experimental verification, that in some cases the axial velocity is the same as that of the axi-symmetric free turbulent jet. In this case the axial velocity of the vortex is given by (Faris, Reference 16)

$$w = W(1 + \beta_{30}) , \quad \frac{\mathcal{R}}{R} \leq 1, \quad (11)$$

$$w = 0 , \quad \frac{\mathcal{R}}{R} \geq 1. \quad (12)$$

Following Long (Reference 18) the kinematic momentum transfer in the axial direction is assumed to be constant; thus,

$$\frac{d}{dz} \int_0^\infty \left(w^2 + \frac{p}{\rho} \right) r \, dr = 0 .$$
(13)

Substitution of w and $\frac{p}{\rho}$ from equations (9), (10), (11), and (12) yields (Appendix B)

$$\frac{d}{dz} (WR) = 0 ,$$
(14)

or,

$$WR = \text{constant} = \pm 2.26 \sqrt{K'} .$$
(15)

The plus sign is to be taken for source flow and the minus for sink flow. Using (15), the axial velocity from (11) and (12) becomes

$$w = \pm \frac{2.26 \sqrt{K'}}{R} \left(1 + \beta_{30} \right) , \quad \frac{r}{R} \leq 1 ,$$
(16)

$$w = 0 , \quad \frac{r}{R} \geq 1 .$$
(17)

Radial Velocity

Using the axial velocity from (16) and (17), the radial velocity may be obtained by integrating the continuity equation:

$$\frac{1}{r}\frac{\partial}{\partial r}(ru) + \frac{\partial w}{\partial z} = 0 . \tag{18}$$

Thus,

$$u = -\frac{1}{r}\int \frac{\partial w}{\partial z} r\, dr + \frac{1}{r} f(z) . \tag{19}$$

Substitution of w from (16) and (17) and application of the boundary condition at $r = 0 : u = 0$ yields (Appendix D)

$$u = \pm 2.26\sqrt{K'}\,\frac{1}{R}\frac{dR}{dz}\frac{1}{\left(\frac{r}{R}\right)}\left[\left(\frac{r}{R}\right)^2(1+\beta_{30}) - \frac{1}{4}\left(\frac{r}{R}\right)^2\right.$$

$$\left. + \frac{1}{4\pi}\sin\pi\left(1-\frac{r}{R}\right)^2 - \frac{1}{2}T\left(\frac{r}{R}\right) + 0.187\right] , \quad \frac{r}{R} \le 1, \tag{20}$$

$$u = \pm\left(-0.142\sqrt{K'}\,\frac{dR}{dz}\right)\frac{1}{r} , \quad \frac{r}{R} \ge 1. \tag{21}$$

The function $T\left(\frac{r}{R}\right)$ is given by

$$T\left(\frac{r}{R}\right) \equiv \sum_{m=0}^{\infty} \frac{(-1)^m \pi^{2m}}{(2m)!\,(4m+1)}\left(1-\frac{r}{R}\right)^{4m+1} , \tag{22}$$

and is plotted in Figure 10.

Boundary Layer Radius

It now remains to determine $R(z)$. According to Newman (Reference 14) and Squire (Reference 19) the kinematic viscosity may be replaced by a turbulent eddy viscosity ϵ which is a function of K and Γ, and is constant throughout the vortex to a good approximation. Employing the usual boundary layer approximation for vortex flow (Long, Reference 18), the axial Navier-Stokes equation then becomes

$$\mu \frac{\partial w}{\partial r} + w \frac{\partial w}{\partial z} = -\frac{1}{\rho} \frac{\partial p}{\partial z} + \epsilon \left(\frac{\partial^2 w}{\partial r^2} + \frac{1}{r} \frac{\partial w}{\partial r} \right). \quad (23)$$

Evaluated at $r = 0$, (23) becomes

$$\left(w \frac{\partial w}{\partial z} \right)_0 = -\frac{1}{\rho} \left(\frac{\partial p}{\partial z} \right)_0 + \epsilon \left[\left(\frac{\partial^2 w}{\partial r^2} \right)_0 + \left(\frac{1}{r} \frac{\partial w}{\partial r} \right)_0 \right], \quad (24)$$

Since $\mu = 0$ at $r = 0$. Evaluation of these $r = 0$ limits from equations (9) and (16) and substitution in (24) yields (Appendix F)

$$\left[5.11\, K - 11.58 \left(\frac{\Gamma}{2\pi} \right)^2 \right] \frac{dR}{dz} = \pm\, 9.04\, \pi^2 \sqrt{K}\, \epsilon . \quad (25)$$

Integrating,

$$R = \pm \left[\frac{9.04\, \pi^2 \sqrt{K}\, \epsilon}{5.11\, K - 11.58 \left(\frac{\Gamma}{2\pi} \right)^2} \right] z + \text{constant.} \quad (26)$$

Again, the plus sign applies to source flow and the minus to sink flow. As stated before, the eddy viscosity ϵ is also a function of K and Γ. This linear dependence of R on Z is in agreement with Long (Reference 12) and Gartshore (Reference 11).

The constant of integration in (26) would be the radius of an orifice at $Z = 0$ if the boundary layer approximations were valid at $Z = 0$. However, near the orifice, the partial derivatives with respect to Z cannot be neglected, and (26) does not apply exactly. Because of this and the existance of a boundary layer next to the wall of the orifice, the constant in (26) will be slightly less than the radius of the orifice.

It can be seen from (26) that in the case of source flow (jet with circulation) dR/dZ becomes infinite if

$$\frac{\Gamma}{2\pi} = \sqrt{\frac{5.11\,K}{11.58}} = 0.665\sqrt{K}, \qquad (27)$$

and for values of $\frac{\Gamma}{2\pi}$ greater than $0.665\sqrt{K}$, dR/dZ is negative. Also, for sink flow (common sink vortex) dR/dZ is negative for values of $\frac{\Gamma}{2\pi}$ less than $0.665\sqrt{K}$. Therefore, since only positive values of dR/dZ are realistic, equation (26) applies only to source flow with zero or small circulation as compared with the kinematic momentum and to sink flow with strong circulation.

Non-Dimensional Equations and Certain Characteristic Values from the Above Equations

Figures 11, 12, and 13 show typical variation of the N, w, and u profiles in the axial direction. To facilitate comparison with

experimental data, the following values are obtained from equations (5),
(9), (16), and (20).

$$\left(\frac{r}{R}\right)_{N_{max}} = 0.386 \; , \; \left(\frac{r}{R}\right)_{\frac{w}{W}=0.5} = 0.292 \; , \; \left(\frac{r}{R}\right)_{\mu_{min}} = 0.190$$

$$\left(\frac{r}{R}\right)_{\mu_{max}} = 0.750 \; , \; \left(\frac{r}{R}\right)_{\mu=0} = 0.412 \; .$$

(28)

$$N_{max} = 1.781 \frac{\Gamma}{2\pi R} \; ,$$

$$\mu_{max} = \pm\left(-0.1727\sqrt{K'}\frac{1}{R}\frac{dR}{dz}\right) ,$$

(29)

$$\frac{N}{N_{max}} = -0.561 \frac{\beta_{3D}}{\left(\frac{r}{R}\right)} \; , \quad \frac{r}{R} = 0.386 \frac{r}{R_{N_{max}}} ,$$

(30)

$$\frac{p - p_\infty}{\frac{1}{2}\rho N_{max}^2} = 0.630\left[F\left(\frac{r}{R}\right) - 5.79\right], \quad \frac{r}{R} = 0.386 \frac{r}{R_{N_{max}}} ,$$

(31)

$$\frac{w}{W} = 1 + \beta_{3D} \; , \quad \frac{r}{R} = 0.292 \frac{r}{R_{\frac{w}{W}=0.5}} ,$$

(32)

$$\frac{\mu}{\mu_{max}} = -13.10 \frac{1}{\left(\frac{r}{R}\right)}\left[\left(\frac{r}{R}\right)^2(1+\beta_{3D}) - \frac{1}{4}\left(\frac{r}{R}\right)^2\right.$$

(33)

$$\left. + \frac{1}{4\pi}\sin\pi\left(1-\frac{r}{R}\right)^2 - \frac{1}{2}T\left(\frac{r}{R}\right) + 0.187\right], \quad \frac{r}{R} = 0.750 \frac{r}{R_{\mu_{max}}} \; .$$

Equations (30), (31), (32), and (33) are plotted in Figures 14, 15,
16, and 17.

Application to Wing-Tip Vortex

In the case of the wing-tip vortex, the axial velocity outside the boundary layer is not zero as in the previous case. Therefore, using coordinates fixed relative to the wing with z positive behind the wing, the axial velocity deficiency rather than the axial velocity is assumed to be a similar function of $\frac{r}{R}$:

$$\frac{W_\infty - w}{W_\infty - W} = 1 + \beta_{3D} \quad , \quad \frac{r}{R} \leq 1,$$

$$w = W_\infty \quad , \quad \frac{r}{R} \geq 1.$$

(34)

After Newman (Reference 14) all the wing wake is assumed to be drawn into the vortex, an assumption which is not justified near the wing but becomes increasingly accurate as z increases. The profile drag of the wing is then given by the deficit of longitudinal momentum within the vortex:

$$D_0 = 2\pi\rho \int_0^\infty w \, (W_\infty - w) \, r \, dr.$$

(35)

Assuming $(W_\infty - w) \ll W_\infty$ (Newman, Reference 14), equation (35) may be written

$$D_0 = 2\pi\rho \int_0^\infty W_\infty \, (W_\infty - w) \, r \, dr.$$

(36)

Substitution for $W_\infty - w$ from (34) and integration (Appendix G) yields

$$D_0 = 0.126 \, \pi \rho \, R^2 \, W_\infty \, (W_\infty - W).$$

(37)

Therefore, (34) becomes

$$W_\infty - w = \left(\frac{D_0}{0.126 \, \pi \rho \, W_\infty} \right) \frac{1}{R^2} (1 + \beta_{30}) \ , \quad \frac{r}{R} \leq 1,$$

(38)

$$w = W_\infty \ , \quad \frac{r}{R} \geq 1.$$

Using the $r = 0$ limits from Appendix H, the axial Navier-Stokes equation (24) becomes

$$\left[2 \left(\frac{D_0}{0.126 \, \pi \rho} \right) + 11.58 \left(\frac{\Gamma}{2\pi} \right)^2 \right] \frac{dR}{dz}$$

$$= 4\pi^2 \epsilon \left(\frac{D_0}{0.126 \, \pi \rho \, W_\infty} \right) \frac{1}{R}.$$

(39)

Integrating,

$$R^2 = \left[\frac{\dfrac{4\pi^2 D_0 \, \epsilon}{0.063 \, \pi \rho \, W_\infty}}{\dfrac{D_0}{0.063 \, \pi \rho} + 11.58 \left(\frac{\Gamma}{2\pi} \right)^2} \right] z \ + \quad \text{constant.}$$

(40)

Thus, the radius of the boundary layer is proportional to the square root of z in the case of the wing-tip vortex, rather than to the first power as in the source or sink type vortex. This conclusion was also reached by Gasparek and Dosanjh (Reference 15) and Squire (Reference 19).

There is no restriction on the circulation in the wing-tip vortex, all values of Γ being possible according to (40). It should be noted that Newman (Reference 14) assumed small axial velocity deficiency _and_ small tangential velocity compared with the remote axial velocity. Here only small axial velocity deficiency has been assumed.

Experimental data taken in the wing-tip vortex behind a NACA 0009 airfoil in a wind tunnel by Gasparek and Dosanjh (Reference 15) is compared with the theory of this paper in Figures 18 and 19. Though the scatter is understandably great, the agreement is generally good. As was predicted, the agreement between theory and experiment becomes greater as the distance from the wing increases.

Application to Axi-Symmetric Free Turbulent Jet

If $\Gamma = 0$, equation (26) applies to the axi-symmetric free turbulent jet:

$$R = \frac{17.42\,\epsilon}{\sqrt{K'}}\,Z \quad + \quad \text{constant.} \tag{41}$$

According to Schlichting (Reference 20), dR/dZ for the axi-symmetric free turbulent jet is independent of the kinematic momentum and is equal to 0.29. This value was confirmed by Faris (Reference 16). Therefore, from (41)

$$\frac{17.42\,\epsilon}{\sqrt{K'}} = 0.29 , \tag{42}$$

or,

$$\epsilon = 0.0166 \sqrt{K'} . \tag{43}$$

Schlichting (Reference 20, p. 608) gives

$$\epsilon = 0.0161 \sqrt{K'} . \tag{44}$$

The close agreement between (43) and (44) confirms the use of the axial Navier-Stokes equation to determine $R(z)$.

THE CONFINED TURBULENT SINK TYPE VORTEX

Extension of the Free Vortex Theory

The theory of the preceding chapter applies only to free vortices.
The introduction of confining walls produces pronounced changes in
the vortex as can be seen in Figure 20 where experimental measurements
of the tangential velocity of a vortex confined in the tube described in
Chapter II are compared with the free vortex theory.

It was found in the preliminary measurements that when the plate
with the hole in it was removed from the tube, the introduction of smoke
showed no characteristic vortex core, and the tangential velocity of the
flow was directly proportional to the radius all the way out to the edge
of the boundary layer on the wall of the tube.

Therefore, it was thought that the tangential velocity of the con-
fined sink type vortex produced with the plate in the tube might be described
by a superposition of the free vortex profile and the linear profile:

$$v = -\frac{\Gamma}{2\pi R}\frac{\beta_{30}}{\left(\frac{r}{R}\right)} + k\, r \ . \tag{45}$$

Experimental Results

The experimental results of the measurements through the five
holes at one variac setting are presented in Figures 21A-21E. In
Figures 21C-21E the experimental data is compared with equation 45,
and the agreement can be seen to be quite good over most of the curve.
The circulation Γ decreases and k increases as the distance from
the plate increases. The tangential velocity at the two stations closest
to the plate (Figures 21A and 21B) is not a linear function of the radius
near the centerline as is the case at the other three stations, and,

therefore, equation 45 does not apply near the plate.

The tangential velocity curves all exhibit a characteristic kink just beyond the maximum values. The region of the kink is also the region of departure from equation 45. It is possible that this may be due to a perturbing effect of the probe, for near the centerline audible perturbations occured when the probe was in the static pressure position. Visual observation with smoke also revealed that the presence of the probe caused a slight displacement of the position of the visible core of the vortex.

The axial flow pattern is very complex as can be seen in Figures 22A-22E. Throughout most of the tube there is very little radial flow. Observations with smoke indicated that after the air enters through the vanes it does not move radially into the center but spirals downward along the wall toward the plate. The smoke forms a hollow visible core as shown in Figures 2 and 3. The radial position of the smoke core apparently corresponds to the second zero point in the axial velocity curves. The top of the smoke core intersects the glass plate at almost a right angle so that the core seems independent of the incoming flow. When the source of the smoke was removed, the core of smoke remained in position and only after several minutes was gradually drawn out through the plate.

Observations with a wool tuft indicated that the flow through the hole in the plate is down toward the fan near the edges of the plate. Nearing the centerline the direction of the flow changes to up toward the vanes. It was not possible to determine the direction on the center-line because of the size of the tuft.

Therefore, the following description of the axial flow may be given as drawn in Figure 23 where the axial velocity profiles at each of the five stations and the tube are drawn to scale. The air enters tangentially at the vanes and spirals downward along the wall toward the plate. At the plate, part of the flow moves out through the hole, and part turns and moves upward along the outside of the smoke core toward the vanes. This flow turns at the vanes and joins the incoming downward flow along the wall.

Inside the smoke core the flow is upward toward the vanes next to the core and downward toward the plate near the axis, being zero on the axis. Thus, the axial flow exhibits two co-axial elongated ring vortices, one outside the core and one inside. The inside ring vortex extends through the hole in the plate and has its turning point below the plate.

Observations with an aural stethescope indicated that the flow was weakly turbulent inside a radius of about 0.85 inch and strongly turbulent inside a radius of 0.30 inch, the transition from weak to strong being gradual.

The results of the measurements at different variac settings are presented in Figures 24 and 25. As can be seen the flow pattern is the same at all three settings, only the magnitudes of the velocities being affected.

CONCLUSIONS

The use of the turbulent wake function $\mathcal{R}_{3D}$ and the boundary layer turbulent entrainment analysis, which correctly describe the axi-symmetric free turbulent jet, has been extended to describe the free turbulent source or sink type vortex. The agreement between theory and experiment in the wing-tip vortex is good, and the theory correctly predicts the value of the turbulent eddy viscosity in the axi-symmetric free turbulent jet. Therefore, it may be said that the theory does correctly describe the free turbulent vortex.

The confined turbulent sink type vortex may be described by a superposition of the tangential velocity of the free vortex and a tangential velocity directly proportional to the radius of the vortex. The agreement between this modified theory and experiment in a vortex confined in a tube is good over most of the curve, and the slight departure from the theory may be due to pertubations caused by the measuring probe.

Experimental measurements revealed that the axial velocity in a confined vortex is quite complex, consisting of two co-axial elongated ring vortices separated by a zero velocity region.

APPENDICES

Table of Contents

Appendix A Evaluation of $\frac{P}{\rho} = \int \frac{N^2}{r} \, dr + f(z)$.

Substituting for N from (5),

$$\frac{P}{\rho} = \left(\frac{\Gamma}{2\pi R}\right)^2 \int \frac{\beta_{3D}^2}{\left(\frac{r}{R}\right)^3} \, d\left(\frac{r}{R}\right) + f(z) \, , \quad \frac{r}{R} \leq 1. \tag{A-1}$$

Graphical integration yields

$$\frac{P}{\rho} = \left(\frac{\Gamma}{2\pi R}\right)^2 F\left(\frac{r}{R}\right) + f(z) \, , \quad \frac{r}{R} \leq 1, \tag{A-2}$$

where

$$F\left(\frac{r}{R}\right) \equiv \int_0^{r/R} \frac{\beta_{3D}^2}{\left(\frac{r}{R}\right)^3} \, d\left(\frac{r}{R}\right), \tag{A-3}$$

and is plotted in Figure 9.

Outside the boundary layer, N is given by (6), and the pressure by

$$\frac{P}{\rho} = \left(\frac{\Gamma}{2\pi}\right)^2 \int \frac{dr}{r^3} + g(z) \, , \quad \frac{r}{R} \geq 1. \tag{A-4}$$

Integrating,

$$\frac{P}{\rho} = -\frac{1}{2}\left(\frac{\Gamma}{2\pi}\right)^2 \frac{1}{r^2} + g(z) \, , \quad \frac{r}{R} \geq 1. \tag{A-5}$$

But at $\pi = \infty$, $p = P_\infty$ so that

$$g(z) = \frac{P_\infty}{\rho} .$$ (A-6)

Therefore,

$$\frac{p}{\rho} = -\frac{1}{2}\left(\frac{\Gamma}{2\pi\pi}\right)^2 + \frac{P_\infty}{\rho} , \quad \frac{\pi}{R} \geq 1.$$ (A-7)

Equations (A-2) and (A-7) must be equal at $\pi = R$:

$$\left(\frac{\Gamma}{2\pi R}\right)^2 F(1) + f(z) = -\frac{1}{2}\left(\frac{\Gamma}{2\pi R}\right)^2 + \frac{P_\infty}{\rho} ,$$ (A-8)

and, therefore, since $F(1) = 5.29$,

$$f(z) = \frac{P_\infty}{\rho} - 5.79\left(\frac{\Gamma}{2\pi R}\right)^2.$$ (A-9)

Substituting (A-9) in (A-2),

$$\frac{p}{\rho} = \frac{P_\infty}{\rho} + \left(\frac{\Gamma}{2\pi R}\right)^2\left[F\left(\frac{\pi}{R}\right) - 5.79\right] , \quad \frac{\pi}{R} \leq 1.$$ (A-10)

Appendix B Evaluation of $\frac{d}{dz} \int_0^\infty \left(w^2 + \frac{p}{\rho} \right) r \, dr = 0.$

From (11) and (12),

$$\frac{d}{dz} \int_0^\infty w^2 r \, dr = \frac{d}{dz} \left[W^2 R^2 \int_0^1 (1 + \beta_{30})^2 \left(\frac{r}{R} \right) d \left(\frac{r}{R} \right) \right], \qquad \text{(B-1)}$$

since $w = 0$ for $r > R$. From Appendix C,

$$\int_0^1 (1 + \beta_{30})^2 \left(\frac{r}{R} \right) d \left(\frac{r}{R} \right) = 0.0311. \qquad \text{(B-2)}$$

Therefore,

$$\frac{d}{dz} \int_0^\infty w^2 r \, dr = 0.0311 \frac{d}{dz} \left(W^2 R^2 \right). \qquad \text{(B-3)}$$

Also,

$$\frac{d}{dz} \int_0^\infty \frac{p}{\rho} r \, dr = \frac{d}{dz} \int_0^R \frac{p}{\rho} r \, dr + \frac{d}{dz} \int_R^\infty \frac{p}{\rho} r \, dr. \qquad \text{(B-4)}$$

Substituting for $\frac{p}{\rho}$ from (9) and (10),

$$\frac{d}{dz} \int_0^\infty \frac{p}{\rho} r \, dr = \frac{d}{dz} \int_0^R \left\{ \frac{P_\infty}{\rho} + \left(\frac{\Gamma}{2\pi R} \right)^2 \left[F \left(\frac{r}{R} \right) - 5.79 \right] \right\} r \, dr$$

$$+ \frac{d}{dz} \int_R^\infty \left\{ \frac{P_\infty}{\rho} - \frac{1}{2} \left(\frac{\Gamma}{2\pi r} \right)^2 \right\} r \, dr, \qquad \text{(B-5)}$$

or,

$$\frac{d}{dz}\int_0^\infty \frac{p}{\rho} \, r\,dr = \frac{d}{dz}\left[\frac{P_\infty}{\rho}\int_0^\infty r\,dr\right] + \left(\frac{\Gamma}{2\pi}\right)^2 \frac{d}{dz}\int_0'\left[F\left(\frac{r}{R}\right) - 5.79\right]\left(\frac{r}{R}\right)d\left(\frac{r}{R}\right)$$

$$- \frac{1}{2}\left(\frac{\Gamma}{2\pi}\right)^2 \frac{d}{dz}\int_1^\infty \frac{d\left(\frac{r}{R}\right)}{\left(\frac{r}{R}\right)} \quad . \tag{B-6}$$

But the values of all three integrals are constants. Therefore, if P_∞ is not a function of z ,

$$\frac{d}{dz}\int_0^\infty \frac{p}{\rho} \, r\,dr = 0. \tag{B-7}$$

And, therefore,

$$\frac{d}{dz}\int_0^\infty \left(w^2 + \frac{p}{\rho}\right)r\,dr = 0.0311\frac{d}{dz}\left(W^2 R^2\right) = 0, \tag{B-8}$$

or,

$$W R = \text{constant.} \tag{B-9}$$

But the kinematic momentum K is given by

$$K = 2\pi\int_0^\infty w^2 r\,dr, \tag{B-10}$$

or,

$$K = 2\pi(0.0311)W^2 R^2 . \tag{B-11}$$

Therefore, from (B-9) and (B-11),

$$WR = \pm 2.26 \sqrt{K'} = \text{constant.} \tag{B-12}$$

The plus sign is to be taken for source flow and the minus for sink flow.

Appendix C Evaluation of $I = \int_0^1 (1 + \beta_{3D})^2 \left(\frac{r}{R}\right) d\left(\frac{r}{R}\right)$.

Using the approximate form of β_{3D} from (3),

$$I = \frac{1}{4}\int_0^1 \left[1 - \cos \pi \left(1 - \frac{r}{R}\right)^2 \right]^2 \left(\frac{r}{R}\right) d\left(\frac{r}{R}\right) . \tag{C-1}$$

Let $\mu = \left(1 - \frac{r}{R}\right)$:

$$I = \frac{1}{4}\int_0^1 (1 - \cos \pi \mu^2)^2 (1 - \mu) d\mu$$

$$= \frac{3}{8}\int_0^1 (1-\mu) d\mu - \frac{1}{2}\int_0^1 \cos \pi \mu^2 d\mu + \frac{1}{2}\int_0^1 \mu \cos \pi \mu^2 d\mu \tag{C-2}$$

$$+ \frac{1}{8}\int_0^1 \cos 2\pi \mu^2 d\mu - \frac{1}{8}\int_0^1 \mu \cos 2\pi \mu^2 d\mu .$$

Expanding the cosine,

$$\int_0^1 \cos \pi \mu^2 d\mu = \sum_{m=0}^{\infty} \int_0^1 \frac{(-1)^m \pi^{2m}}{(2m)!} \mu^{4m} d\mu$$

$$= \sum_{m=0}^{\infty} \frac{(-1)^m \pi^{2m}}{(2m)!(4m+1)} \mu^{4m+1} \Big|_0^1 . \tag{C-3}$$

Therefore,

$$I = -\frac{3}{16}(1-\mu)^2 \Big|_0^1 - \frac{1}{2}\sum_{m=0}^{\infty} \frac{(-1)^m \pi^{2m}}{(2m)!(4m+1)} \mu^{4m+1} \Big|_0^1$$

$$+ \frac{1}{4\pi}\sin \pi \mu^2 \Big|_0^1 + \frac{1}{8}\sum_{m=0}^{\infty} \frac{(-1)^m (2\pi)^{2m}}{(2m)!(4m+1)} \mu^{4m+1} \Big|_0^1 \tag{C-4}$$

$$- \frac{1}{32\pi}\sin 2\pi \mu^2 \Big|_0^1 ,$$

or, evaluating the series,

$$I = \frac{3}{16} - \frac{1}{2}(0.374) + \frac{1}{8}(0.245) = 0.0311 . \tag{C-5}$$

Appendix D Evaluation of $\mu = -\frac{1}{2}\int \frac{\partial \bar{\mu}}{\partial z} \, \imath \, d\imath + \frac{f(z)}{\imath}$

From (16),

$$\frac{\partial \bar{\mu}}{\partial z} = \pm 2.26 \sqrt{K'} \left[-\frac{1}{R^2}\frac{dR}{dz}(1+\beta_{30}) + \frac{1}{R}\beta_{30}' \, \frac{d\left(\frac{\imath}{R}\right)}{dz} \right]$$

$$= \pm 2.26 \sqrt{K'} \left\{ -\frac{1}{R^2}\frac{dR}{dz}\left[(1+\beta_{30}) + \frac{\imath}{R}\beta_{30}' \right] \right\}, \quad \frac{\imath}{R} \leq 1 \tag{D-1}$$

Therefore,

$$\imath\mu = \pm 2.26 \sqrt{K'} \frac{dR}{dz} \int \left[(1+\beta_{30}) + \frac{\imath}{R}\beta_{30}' \right] \left(\frac{\imath}{R}\right) d\left(\frac{\imath}{R}\right)$$

$$+ f(z), \tag{D-2}$$

or,

$$\imath\mu = \pm 2.26 \sqrt{K'} \frac{dR}{dz} \left[\int \left(\frac{\imath}{R}\right) d\left(\frac{\imath}{R}\right) + \int \beta_{30} \left(\frac{\imath}{R}\right) d\left(\frac{\imath}{R}\right) \right.$$

$$\left. + \int \beta_{30}' \left(\frac{\imath}{R}\right)^2 d\left(\frac{\imath}{R}\right) \right] + f(z). \tag{D-3}$$

Integrating the last integral by parts:

$$\int \beta_{30}' \left(\frac{\imath}{R}\right)^2 d\left(\frac{\imath}{R}\right) = \beta_{30} \left(\frac{\imath}{R}\right)^2 - 2\int \beta_{30} \left(\frac{\imath}{R}\right) d\left(\frac{\imath}{R}\right). \tag{D-4}$$

Therefore,

$$\dot{r}u = \pm 2.26\sqrt{K'}\frac{dR}{dz}\left[\frac{1}{2}\left(\frac{r}{R}\right)^2 + \beta_{3D}\left(\frac{r}{R}\right)^2\right.$$

$$\left. - \int \beta_{3D}\left(\frac{r}{R}\right)d\left(\frac{r}{R}\right)\right] + f(z) \tag{D-5}$$

The integral is evaluated in the same manner as in Appendix C so that

$$\int \beta_{3D}\left(\frac{r}{R}\right)d\left(\frac{r}{R}\right) = -\frac{1}{4}\left(\frac{r}{R}\right)^2 - \frac{1}{4\pi}\sin\pi\left(1 - \frac{r}{R}\right)^2$$

$$+ \frac{1}{2}\sum_{m=0}^{\infty}\frac{(-1)^m\pi^{2m}}{(2m)!(4m+1)}\left(1 - \frac{r}{R}\right)^{4m+1} \tag{D-6}$$

Therefore,

$$\dot{r}u = \pm 2.26\sqrt{K'}\frac{dR}{dz}\left[\left(\frac{r}{R}\right)^2(1+\beta_{3D}) - \frac{1}{4}\left(\frac{r}{R}\right)^2\right.$$

$$\left. + \frac{1}{4\pi}\sin\pi\left(1 - \frac{r}{R}\right)^2 - \frac{1}{2}T\left(\frac{r}{R}\right)\right] + f(z), \quad \frac{r}{R} \leq 1, \tag{D-7}$$

where

$$T\left(\frac{r}{R}\right) \equiv \sum_{m=0}^{\infty}\frac{(-1)^m\pi^{2m}}{(2m)!(4m+1)}\left(1 - \frac{r}{R}\right)^{4m+1}.$$

Finally,

$$u = \pm 2.26\sqrt{K'}\frac{1}{R}\frac{dR}{dz}\frac{1}{\left(\frac{r}{R}\right)}\left[\left(\frac{r}{R}\right)^2(1+\beta_{3D}) - \frac{1}{4}\left(\frac{r}{R}\right)^2\right.$$

$$\left. + \frac{1}{4\pi}\sin\pi\left(1 - \frac{r}{R}\right)^2 - \frac{1}{2}T\left(\frac{r}{R}\right)\right] + \frac{1}{\left(\frac{r}{R}\right)}\frac{f(z)}{R}, \quad \frac{r}{R} \leq 1. \tag{D-8}$$

But at $h = 0$, $\mu = 0$ so that $f(z)$ must satisfy the equation:

$$\pm 2.26 \sqrt{K'} \frac{1}{R} \frac{dR}{dz} \left[-\frac{1}{2} T(0) \right] + \frac{f(z)}{R} = 0. \qquad \text{(D-9)}$$

Therefore, since $T(0) = 0.374$,

$$f(z) = \pm 2.26 \sqrt{K'} \frac{dR}{dz} (0.187), \qquad \text{(D-10)}$$

and (D-8) becomes

$$\mu \doteq \pm 2.26 \sqrt{K'} \frac{1}{R} \frac{dR}{dz} \frac{1}{\left(\frac{h}{R}\right)} \left[\left(\frac{h}{R}\right)^2 (1 + \beta_{30}) - \frac{1}{4} \left(\frac{h}{R}\right)^2 \right.$$

$$\left. + \frac{1}{4\pi} \sin \pi \left(1 - \frac{h}{R}\right)^2 - \frac{1}{2} T\left(\frac{h}{R}\right) + 0.187 \right], \quad \frac{h}{R} \leq 1. \qquad \text{(D-11)}$$

It is shown in Appendix E by application of L'Hospital's rule to (D-11) that μ is indeed zero at $h = 0$.

Outside the boundary layer, $w = 0$ and the continuity equation becomes

$$\frac{\partial}{\partial h} (h\mu) = 0. \qquad \text{(D-12)}$$

Therefore,

$$\mu = \frac{g(z)}{h}, \quad \frac{h}{R} \geq 1. \qquad \text{(D-13)}$$

But (D-11) and (D-13) must be equal at $n = R$:

$$\pm 2.26 \sqrt{K} \; \frac{1}{R} \; \frac{dR}{dz} \left(-0.063\right) = \frac{g(z)}{R} , \qquad \text{(D-14)}$$

since $T(1) = 0$. Therefore,

$$g(z) = \pm \left(-0.142 \sqrt{K} \; \frac{dR}{dz}\right), \qquad \text{(D-15)}$$

and (D-13) becomes

$$\mu = \pm \left(-0.142 \sqrt{K} \; \frac{dR}{dz}\right) \frac{1}{n} , \qquad \frac{n}{R} \geq 1. \qquad \text{(D-16)}$$

Appendix E. Evaluation of $\lim_{\mathcal{R} \to 0} \mu$.

From (D-11),

$$\lim_{\mathcal{R} \to 0} \mu = \pm 2.26 \sqrt{K'} \frac{1}{R} \frac{dR}{dz} \lim_{\frac{\mathcal{R}}{R} \to 0} \frac{1}{\left(\frac{\mathcal{R}}{R}\right)} \left[\left(\frac{\mathcal{R}}{R}\right)^2 (1+\beta_{3D}) \right.$$

$$\left. - \frac{1}{4}\left(\frac{\mathcal{R}}{R}\right)^2 + \frac{1}{4\pi} \sin \pi \left(1 - \frac{\mathcal{R}}{R}\right)^2 - \frac{1}{2} T\left(\frac{\mathcal{R}}{R}\right) + 0.187 \right], \tag{E-1}$$

which by L'Hospital's rule becomes

$$\lim_{\mathcal{R} \to 0} \mu = \pm 2.26 \sqrt{K'} \frac{1}{R} \frac{dR}{dz} \lim_{\frac{\mathcal{R}}{R} \to 0} \left[\left(\frac{\mathcal{R}}{R}\right)^2 \beta_{3D}' + 2\left(\frac{\mathcal{R}}{R}\right)(1+\beta_{3D}) \right.$$

$$\left. - \frac{1}{2}\left(\frac{\mathcal{R}}{R}\right) - \frac{1}{2}\left(1 - \frac{\mathcal{R}}{R}\right)\cos \pi \left(1 - \frac{\mathcal{R}}{R}\right)^2 - \frac{1}{2} T'\left(\frac{\mathcal{R}}{R}\right) \right]. \tag{E-2}$$

But, from Appendix D,

$$T'\left(\frac{\mathcal{R}}{R}\right) = - \sum_{m=0}^{\infty} \frac{(-1)^m \pi^{2m}}{(2m)!} \left(1 - \frac{\mathcal{R}}{R}\right)^{4m} = - \cos \pi \left(1 - \frac{\mathcal{R}}{R}\right)^2. \tag{E-3}$$

Therefore,

$$\lim_{\mathcal{R} \to 0} \mu = 0.$$

Appendix F Evaluation of $\left(w \frac{\partial w}{\partial z}\right)_0$, $\frac{1}{\rho}\left(\frac{\partial p}{\partial z}\right)_0$,

$$\left(\frac{\partial^2 w}{\partial r^2}\right)_0, \quad \left(\frac{1}{r}\frac{\partial w}{\partial r}\right)_0 .$$

From (9), since $F(0) = 0$,

$$\left(\frac{p}{\rho}\right)_0 = \frac{P_\infty}{\rho} - 5.79\left(\frac{\Gamma}{2\pi R}\right)^2 . \tag{F-1}$$

Therefore,

$$\frac{1}{\rho}\left(\frac{\partial p}{\partial z}\right)_0 = 11.58\left(\frac{\Gamma}{2\pi}\right)^2 \frac{1}{R^3}\frac{dR}{dz} . \tag{F-2}$$

From (16), since $\beta_{3D}(0) = 0$,

$$w_0 = \pm \frac{2.26\sqrt{K}}{R} . \tag{F-3}$$

Therefore,

$$\left(w \frac{\partial w}{\partial z}\right)_0 = -\left(\pm \frac{2.26\sqrt{K}}{R}\right)\left(\pm \frac{2.26\sqrt{K}}{R^2}\frac{dR}{dz}\right)$$

$$= -\frac{5.11\,K}{R^3}\frac{dR}{dz} . \tag{F-4}$$

Also, from (16),

$$\frac{\partial w}{\partial z} = \frac{1}{R}\frac{\partial w}{\partial\left(\frac{z}{R}\right)} = \pm \frac{2.26\sqrt{K}}{R^2}\beta_{3D}' . \tag{F-5}$$

Similarly,

$$\frac{\partial^2 w}{\partial z^2} = \pm \frac{2.26\sqrt{K'}}{R^3}\beta_{30}'' \qquad (F-6)$$

Differentiation of (3) yields

$$\beta_{30}'' = \pi \sin \pi \left(1-\frac{z}{R}\right)^2 + 2\pi^2\left(1-\frac{z}{R}\right)^2 \cos \pi \left(1-\frac{z}{R}\right)^2, \qquad (F-7)$$

so that $\beta_{30}''(0) = -2\pi^2.$

Therefore,

$$\left(\frac{\partial^2 w}{\partial z^2}\right)_0 = \pm \left(-\frac{4.52\pi^2\sqrt{K'}}{R^3}\right) \qquad (F-8)$$

Also,

$$\left(\frac{1}{z}\frac{\partial w}{\partial z}\right)_0 = \lim_{\frac{z}{R}\to 0}\left[\pm \frac{2.26\sqrt{K'}}{R^3}\frac{\beta_{30}'}{\left(\frac{z}{R}\right)}\right]$$

$$\qquad (F-9)$$

$$= \pm \frac{2.26\sqrt{K'}}{R^3}\lim_{\frac{z}{R}\to 0}\beta_{30}'',$$

or,

$$\left(\frac{1}{z}\frac{\partial w}{\partial z}\right)_0 = \pm \left(-\frac{4.52\pi^2\sqrt{K'}}{R^3}\right). \qquad (F-10)$$

Appendix G Evaluation of $\int_0^1 (1+\beta_{3D})\left(\frac{z}{R}\right)d\left(\frac{z}{R}\right)$.

Proceeding as in Appendix C,

$$\int_0^1 (1+\beta_{3D})\left(\frac{z}{R}\right)d\left(\frac{z}{R}\right) = \frac{1}{2}\int_0^1 (1-\mu)d\mu$$

$$-\frac{1}{2}\int_0^1 \cos\pi\mu^2 d\mu + \frac{1}{2}\int_0^1 \mu\cos\pi\mu^2 d\mu,$$

(G-1)

or,

$$\int_0^1 (1+\beta_{3D})\left(\frac{z}{R}\right)d\left(\frac{z}{R}\right) = \frac{1}{4} - \frac{1}{2}(0.374) = 0.063.$$

(G-2)

Appendix H Evaluation of $\left(w \frac{\partial w}{\partial z} \right)_0$, $\left(\frac{\partial^2 w}{\partial z^2} \right)_0$,

$$\left(\frac{1}{z} \frac{\partial w}{\partial z} \right)_0 \;,\quad \frac{1}{\rho} \left(\frac{\partial f}{\partial z} \right)_0$$

for wing-tip vortex.

Form (34), since $\beta_{30}(0) = 0$,

$$w_0 = W_\infty - \left(\frac{D_0}{0.126 \, \pi \, \rho \, W_\infty} \right) \frac{1}{R^2} \cong W_\infty \; . \tag{H-1}$$

Therefore,

$$\left(w \frac{\partial w}{\partial z} \right)_0 = 2 \left(\frac{D_0}{0.126 \, \pi \, \rho} \right) \frac{1}{R^3} \frac{dR}{dz} \; . \tag{H-2}$$

Also,

$$\frac{\partial w}{\partial z} = - \left(\frac{D_0}{0.126 \, \pi \, \rho \, W_\infty} \right) \frac{1}{R^3} \beta_{30}' \; , \tag{H-3}$$

$$\frac{\partial^2 w}{\partial z^2} = - \left(\frac{D_0}{0.126 \, \pi \, \rho \, W_\infty} \right) \frac{1}{R^4} \beta_{30}'' \; . \tag{H-4}$$

Therefore, since $\beta_{30}''(0) = -2\pi^2$,

$$\left(\frac{\partial^2 w}{\partial n^2}\right)_c = 2\pi^2 \left(\frac{D_0}{0.126\,\pi\,F\,W_\infty}\right)\frac{1}{R^4} \quad .$$ (H-5)

Also,

$$\left(\frac{1}{n}\frac{\partial w}{\partial n}\right)_0 = -\left(\frac{D_0}{0.126\,\pi\,F\,W_\infty}\right)\frac{1}{R^4} \lim_{\frac{n}{R}\to 0} \frac{\beta_{30}'}{\left(\frac{n}{R}\right)} \quad ,$$ (H-6)

which, as in Appendix F, becomes

$$\left(\frac{1}{n}\frac{\partial w}{\partial n}\right)_0 = 2\pi^2 \left(\frac{D_0}{0.126\,\pi\,F\,W_\infty}\right)\frac{1}{R^4} \quad .$$ (H-7)

The pressure term in unaltered, being given by (F-2) in Appendix F.

BIBLIOGRAPHY

1. Weske, J. R. The Effect of Stretching of a Vortex Core. University of Maryland, Institute for Fluid Dynamics and Applied Mathematics, Technical Note BN-57 (August 1955).

2. Long, R. R. Tornadoes and Dust Whirls. John Hopkins University, Department of Mechanics, TR-10 (ONR) and TR-13 (CWB) (September 1960).

3. Kreith, F. and Margolis, D. Heat Transfer and Friction in Swirling Turbulent Flow. 1958 Heat Transfer and Fluid Mechanics Institute (University of California), Stanford University Press (1958).

4. Kearsey, H. A. and Hibbert, N. S. The Separation of Gases from Liquids by Means of Vortical Flow in a Cylindrical Vessel. U. K. Atomic Energy Authority, AERE CE/R 2628 (August 1958).

5. Ragsdale, R. G. NASA Research on the Hydrodynamics of the Gaseous Vortex Reactor. NASA TN D-288 (September 1960).

6. Lay, J. E. and Lee, B. C. A Study of the Influence of Entry Angle in Vortex Flow Temperature Separation. ASME Paper 60-WA-239 (November 1960).

7. Kerrebrock, J. L. and Meghreblian, R. V. "Vortex Containment for the Gaseous Fission Rocket," Journal of the Aero/Space Sciences, Vol. 28, No. 9 (September 1961).

8. Rosenzweig, M. L. The Vortex Matrix Approach to Gaseous Nuclear Propulsion. Preprint 1735-61, American Rocket Society, New York (May 1961).

9. Lewellen, W. S. "Magnetohydrodynamically Driven Vortices," Proc. of the Heat Transfer and Fluid Mechanics Inst., Stanford University (1960).

10. McCune, J. E. and Donaldson, C. duP. On the Magneto Gas Dynamics of Compressible Vortices. Preprint 1319-60, American Rocket Society, New York (May 1960).

11. Gartshore, I. S. Recent Work in Swirling Incompressible Flow. National Research Council of Canada Aeronautical Report LR-343 (June 1962).

12. Long, R. R. A Vortex in an Infinite Viscous Fluid. John Hopkins University, Department of Mechanics TR 11 (ONR) or TR 14 (CWB) (June 1961).

13. Lewellen, W. S. _A Solution for Three-Dimensional Vortex Flows with Strong Circulation._ Aerospace Corporation Report No. TDR-930 (2210-14) TN-1 (March 1962).

14. Newman, B. G. "Flow in a Viscous Trailing Vortex," _The Aeronautical Quarterly_, Vol. X (May 1959), pp. 149-62.

15. Gasparek, E. P. and Dosanjh, D. S. _Decay of a Viscous Trailing Vortex._

16. Paris, G. N. _Some Entrainment Properties of a Turbulent Axi-Symmetric Jet._ Mississippi State University, Aerophysics Department, Report No. 39 (January 1963).

17. Cornish, J. J., III "Personal Communication" (June 1962).

18. Long, R. R. "Vortex Motion in a Viscous Fluid," _Journal of Meteorology_, Vol. 15, No. 1 (February 1958).

19. Squire, H. B. _The Growth of a Vortex in Turbulent Flow._ U. K. Aeronautical Research Council, Fluid Motion Sub-Committee, FM 2053 (March 1954).

20. Schlichting, H. _Boundary Layer Theory._ McGraw-Hill, New York (1960), 4th ed.

Figure 1

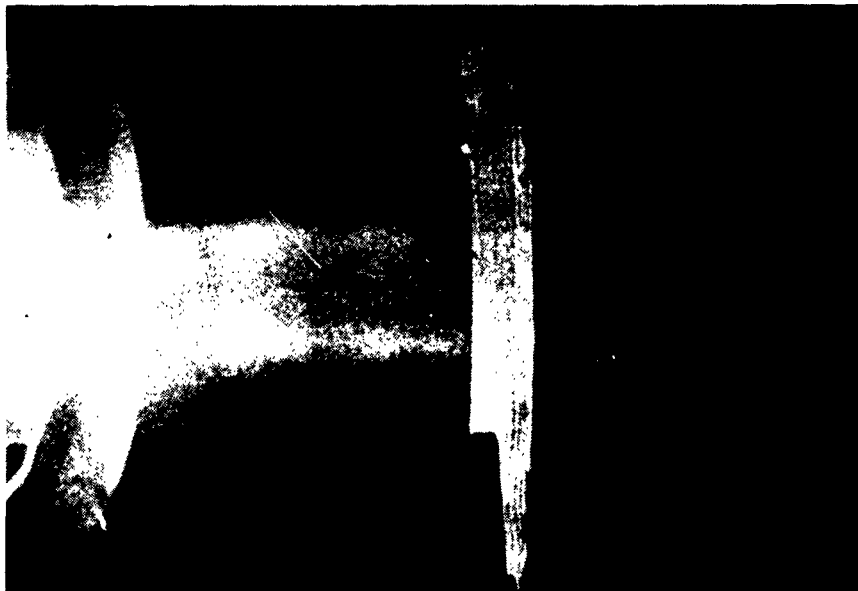GLASS COVER
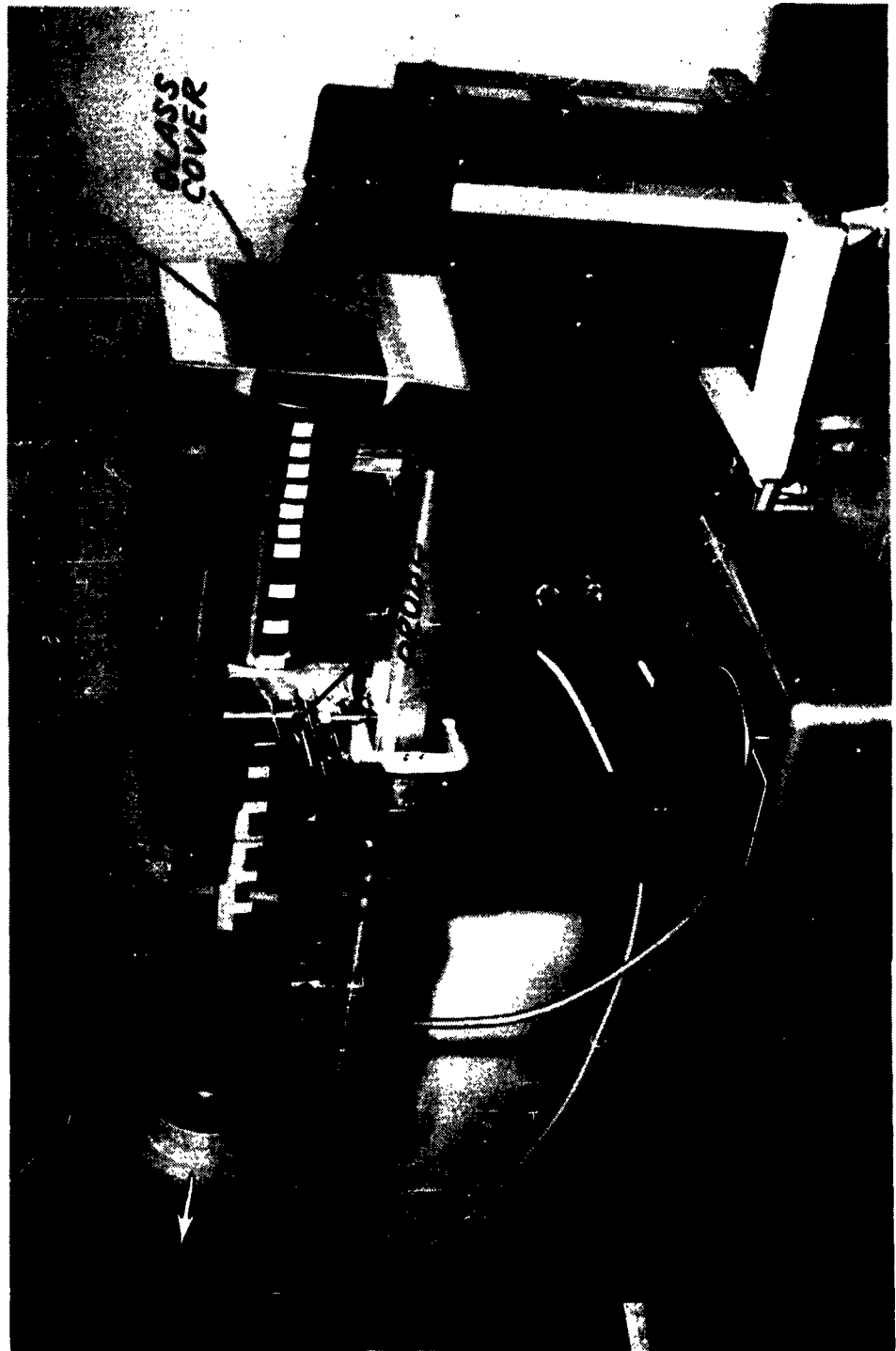
Experimental Apparatus
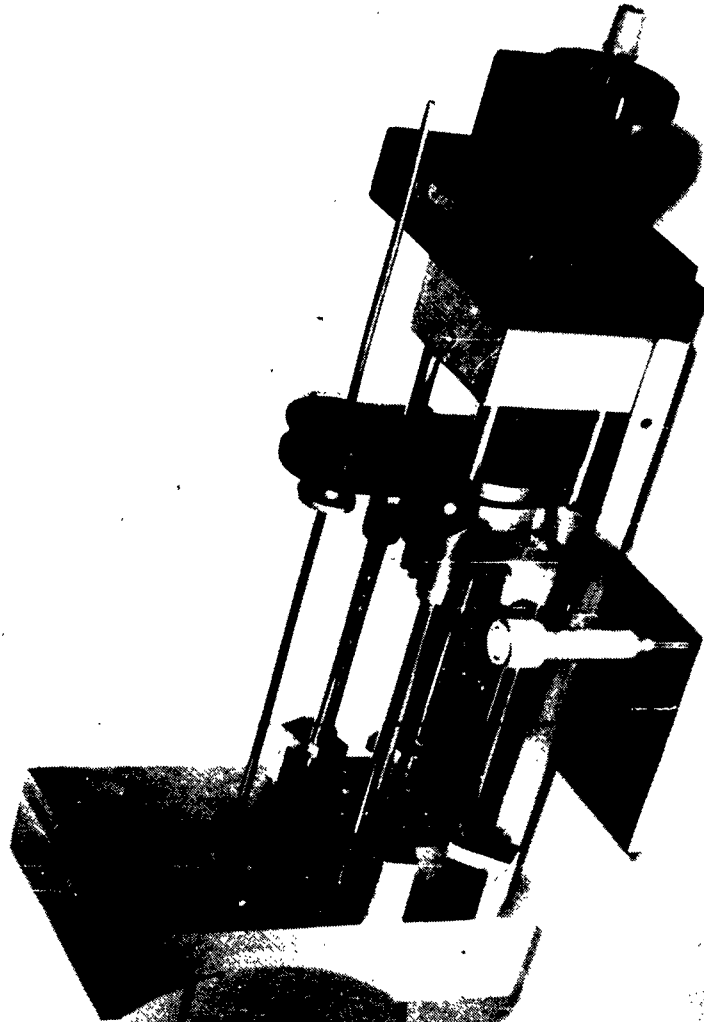
Figure 2   Confined Vortex Core, Side View

Figure 3   Confined Vortex Core, End View

Figure 4

Pressure Probe and Traversing Mechanism

Figure 5

POTENTIAL VORTEX
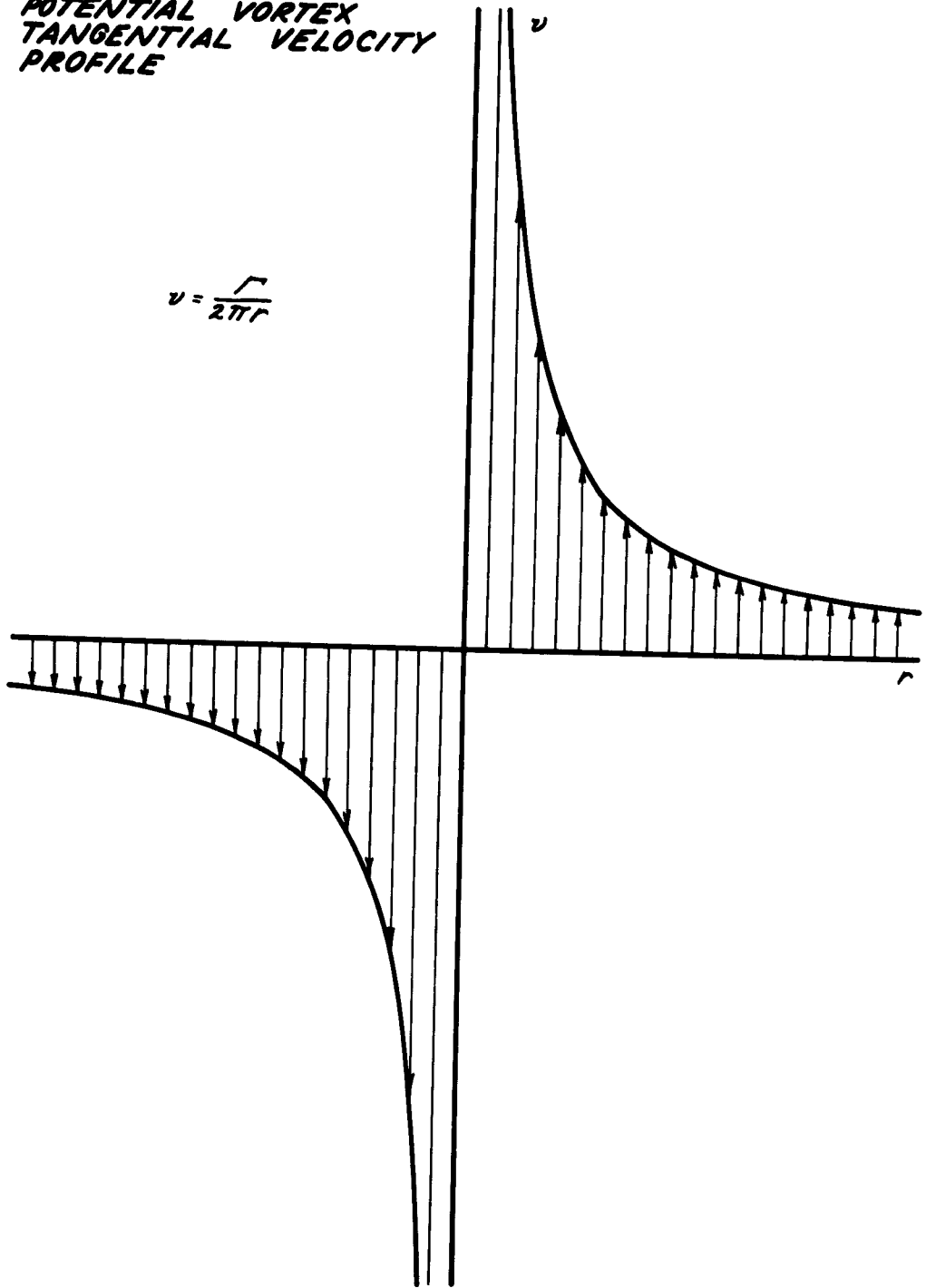TANGENTIAL VELOCITY
PROFILE

$$\nu = \frac{\Gamma}{2\pi r}$$

Figure 6

AXI-SYMMETRIC FREE TURBULENT JET AXIAL VELOCITY

$w = W(1 + \beta_{3D})$
$W = $ CENTER LINE VELOCITY

$\dfrac{w}{W}$

$\dfrac{r}{R}$

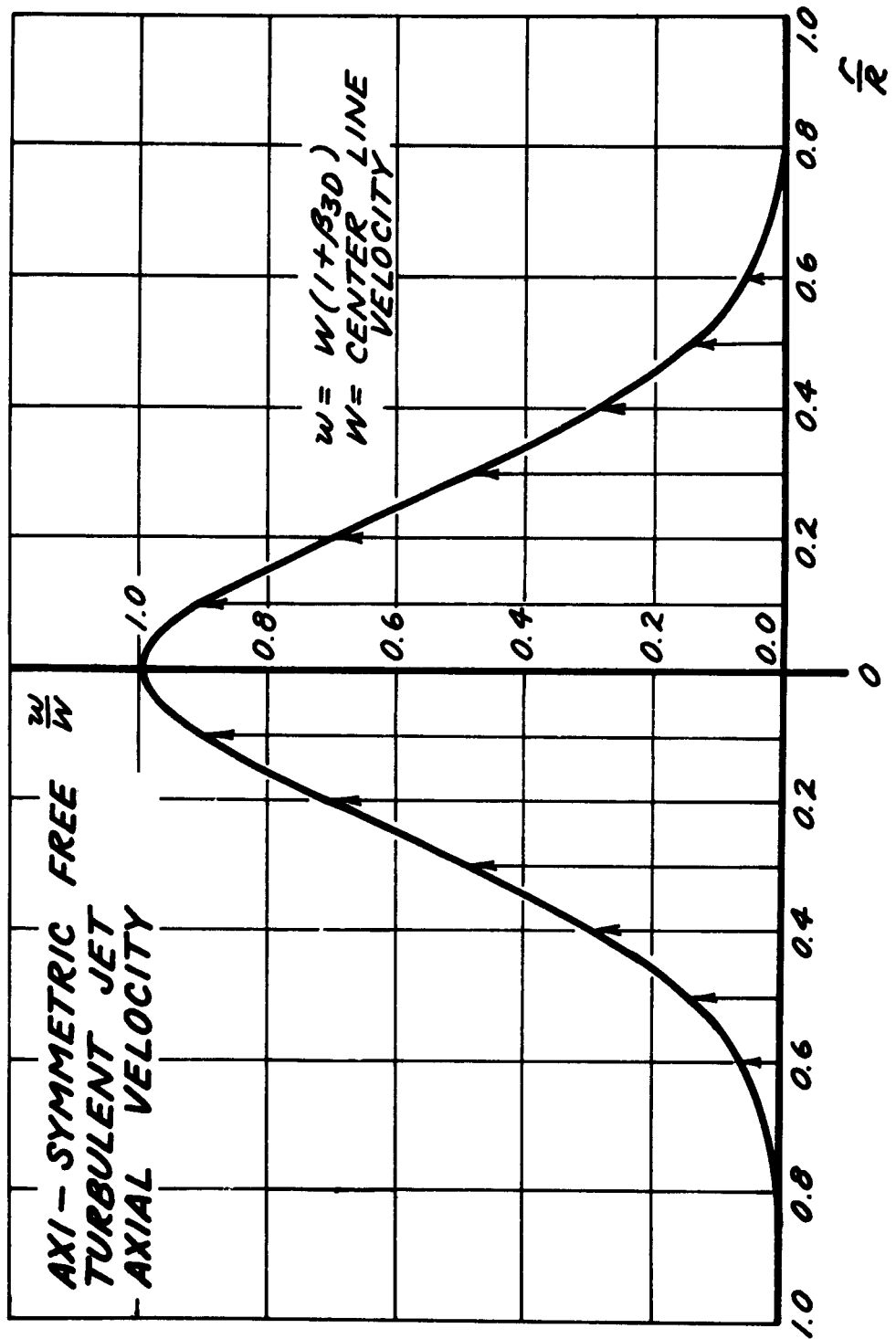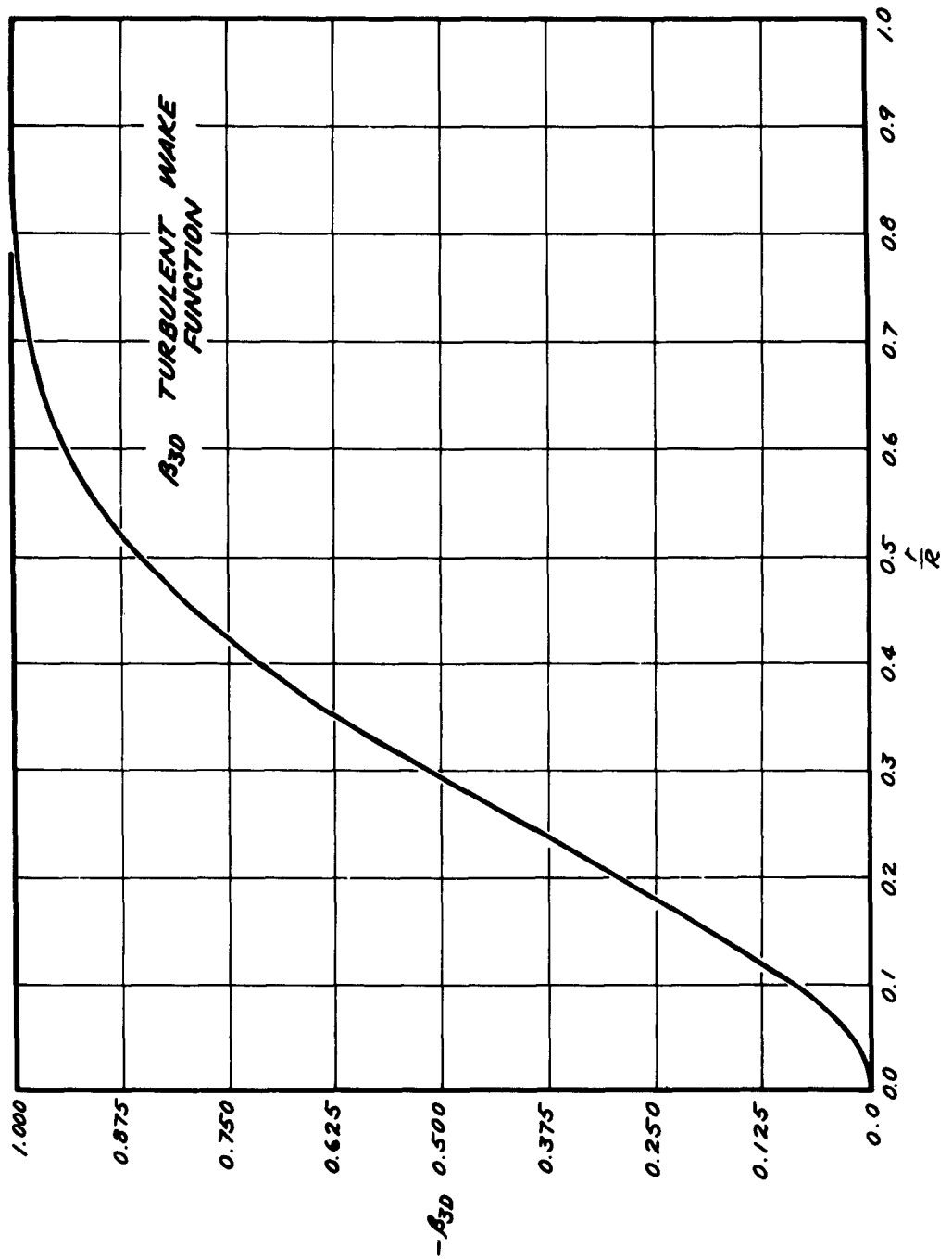# Figure 7

Figure 8

ADDITION OF POTENTIAL
AND ENTRAINED FLOW
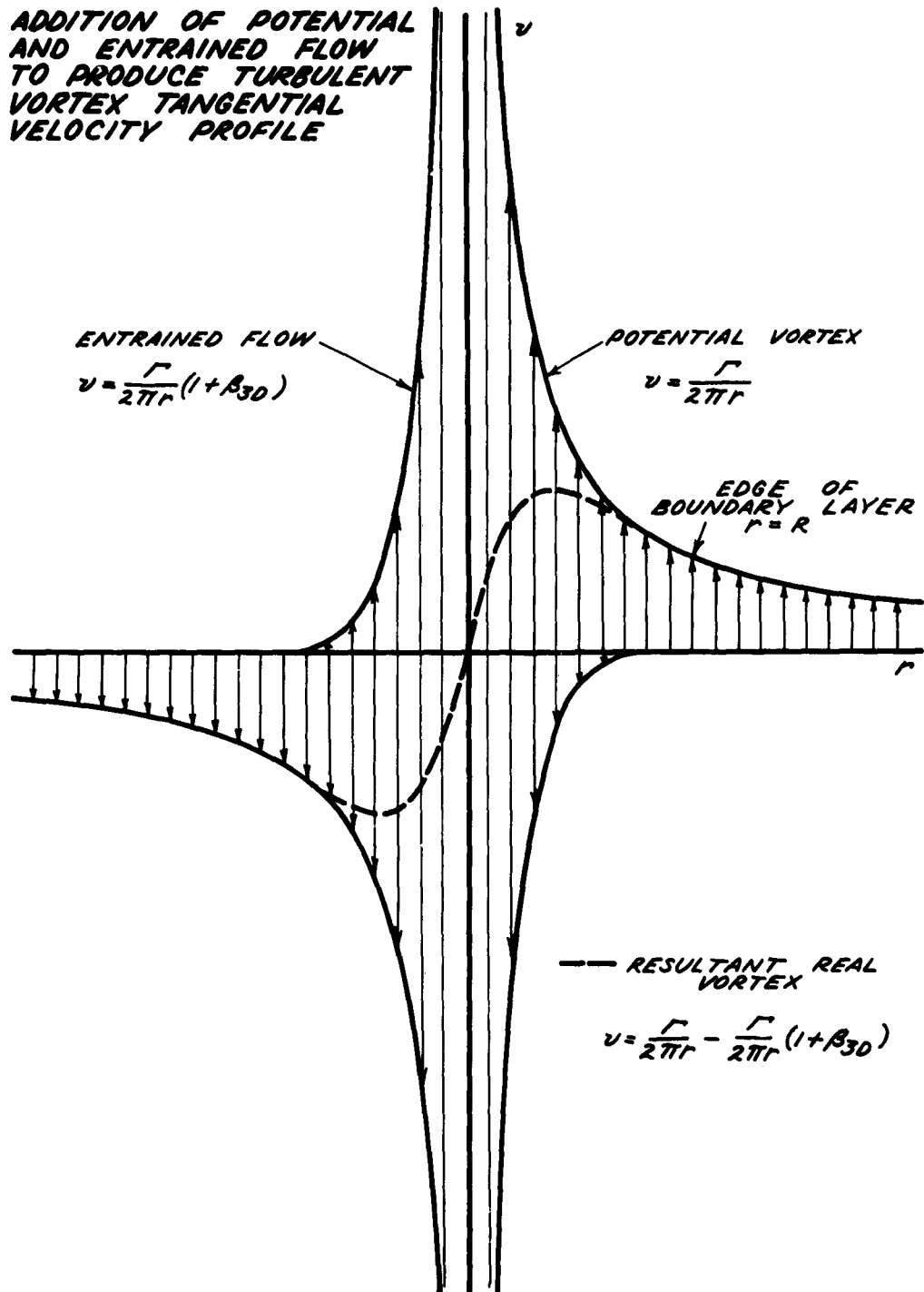TO PRODUCE TURBULENT
VORTEX TANGENTIAL
VELOCITY PROFILE

ENTRAINED FLOW

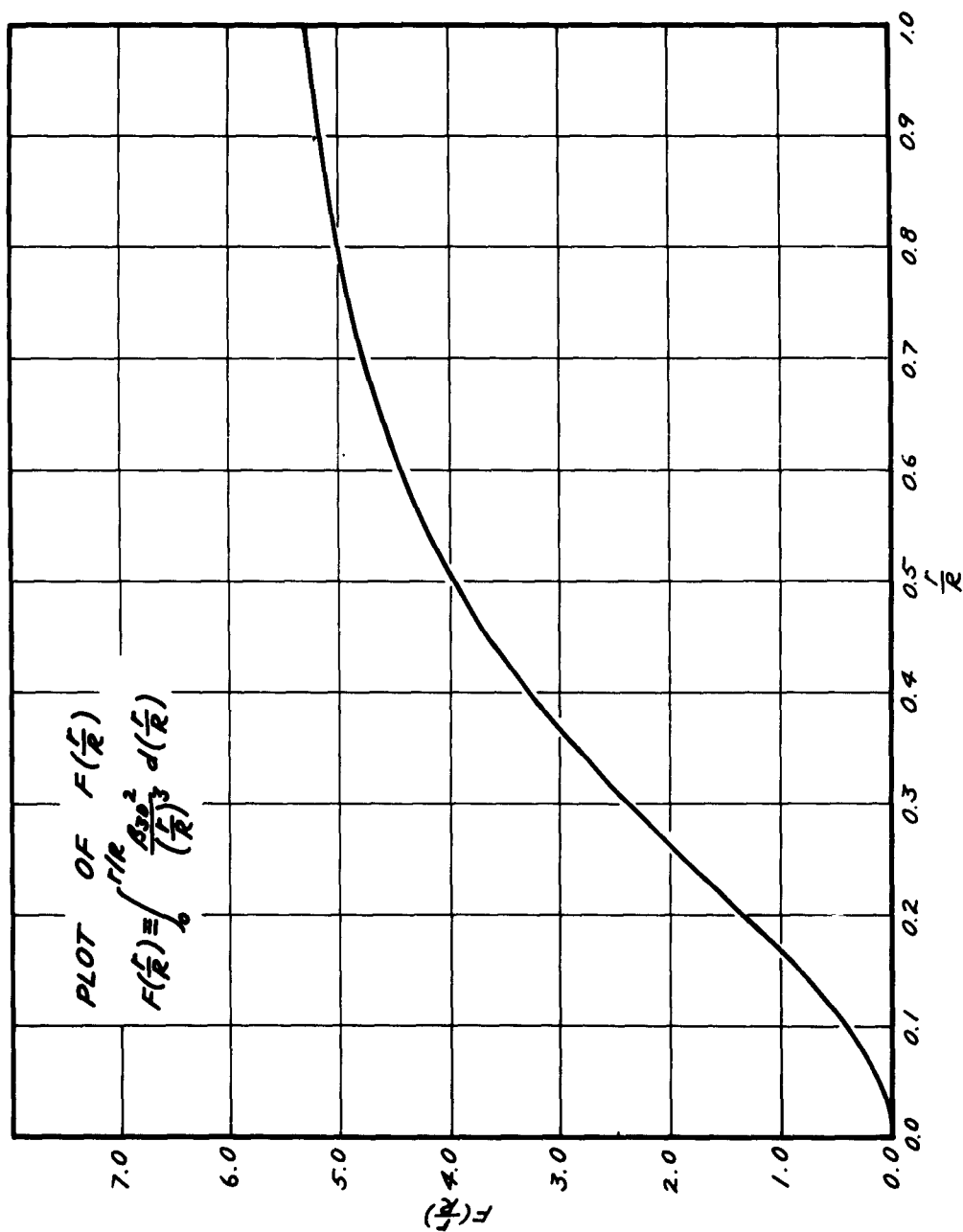$$\nu = \frac{\Gamma}{2\pi r}(1+\beta_{30})$$

POTENTIAL VORTEX

$$\nu = \frac{\Gamma}{2\pi r}$$

EDGE OF
BOUNDARY LAYER
$r = R$

RESULTANT REAL
VORTEX

$$\nu = \frac{\Gamma}{2\pi r} - \frac{\Gamma}{2\pi r}(1+\beta_{30})$$

Figure 9

PLOT OF $F\left(\frac{r}{R}\right)$

$$F\left(\frac{r}{R}\right) = \int_{0}^{r/R} \frac{B_{3D}^{2}}{\left(\frac{r}{R}\right)^{3}} \, d\left(\frac{r}{R}\right)$$

Figure 10

PLOT OF $T\left(\frac{r}{R}\right)$

$$T\left(\frac{r}{R}\right) = \sum_{n=0}^{\infty} \frac{(-1)^n \left(\frac{\pi}{4}\right)^{2n}}{(2n)!(4n+1)} \left(1-\frac{r}{R}\right)^{4n+1}$$

Figure 11

FREE TURBULENT VORTEX
TYPICAL VARIATION OF TANGENTIAL
VELOCITY PROFILES IN THE
AXIAL DIRECTION

$$\nu = -\frac{\Gamma}{2\pi R}\left(\frac{r}{R}\right)$$

POTENTIAL VORTEX PROFILE

$z_{1.5}$

z_2

$z_{1.5}$ (EDGE OF BOUNDARY LAYER, $r = R$)

z_2

z_3

z_3

z_4

z_4

z_5

z_5

z_6

z_6

z_7

z_7

z_8

z_8

z_9

z_9

z_{10}

z_{10}

SCHEMATIC DRAWING OF VORTEX

z_{10}
z_9
z_8
z_7
z_6
z_5
z_4
z_3
z_2
$z_{1.5}$

z

ν

r

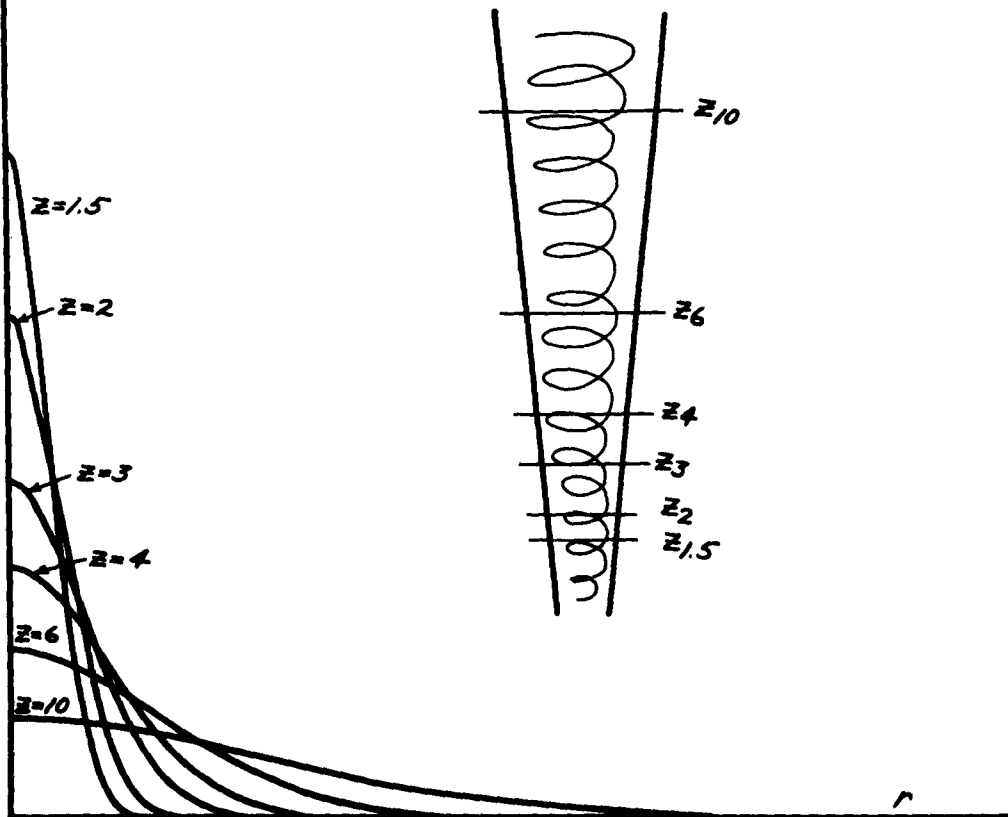# Figure 12

FREE TURBULENT VORTEX
TYPICAL VARIATION OF AXIAL
VELOCITY PROFILES IN THE
AXIAL DIRECTION

$$w = \frac{-2.36\sqrt{K}}{R}(1+P_{30})$$

SCHEMATIC DRAWING
OF VORTEX

Figure 13
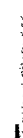

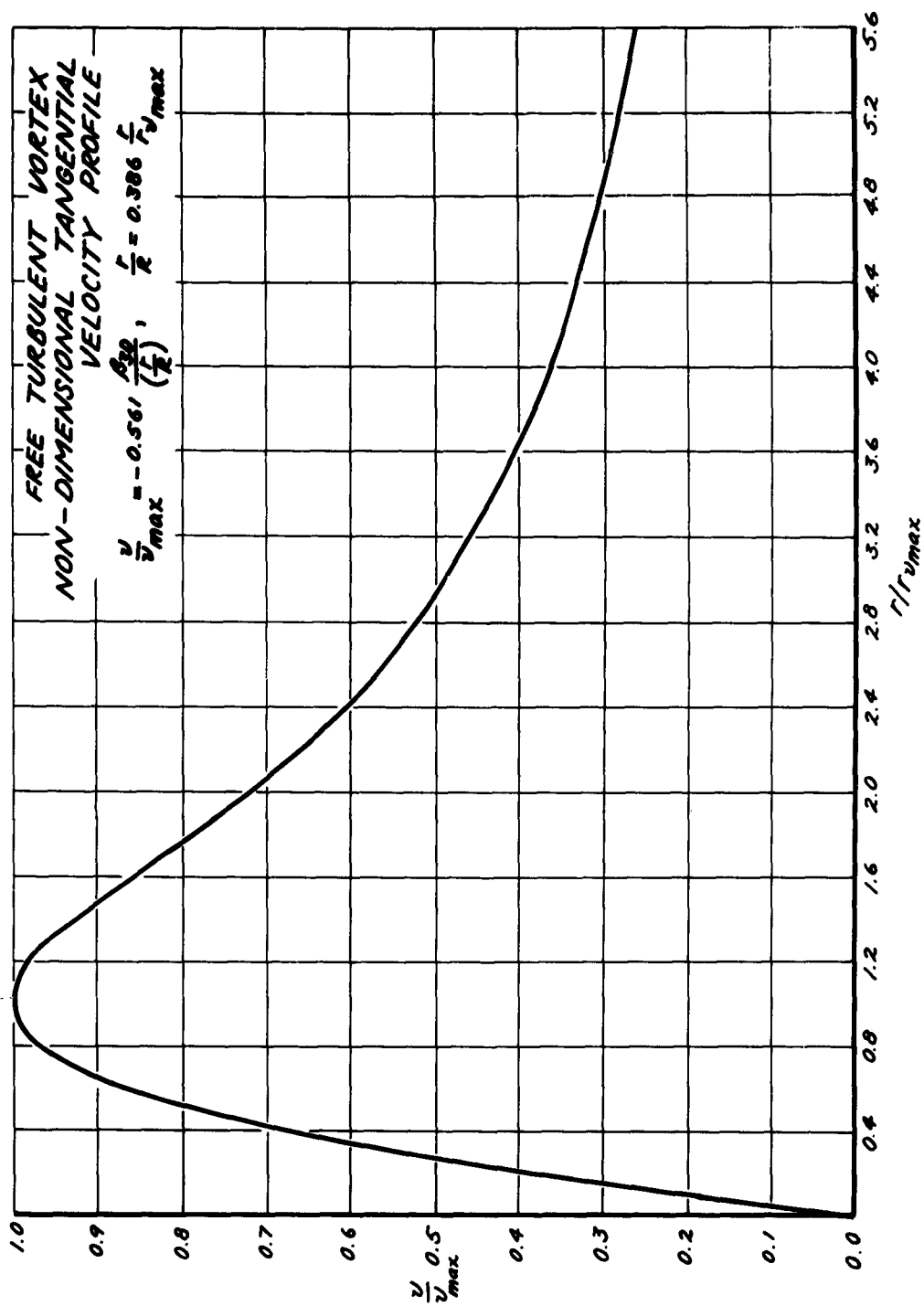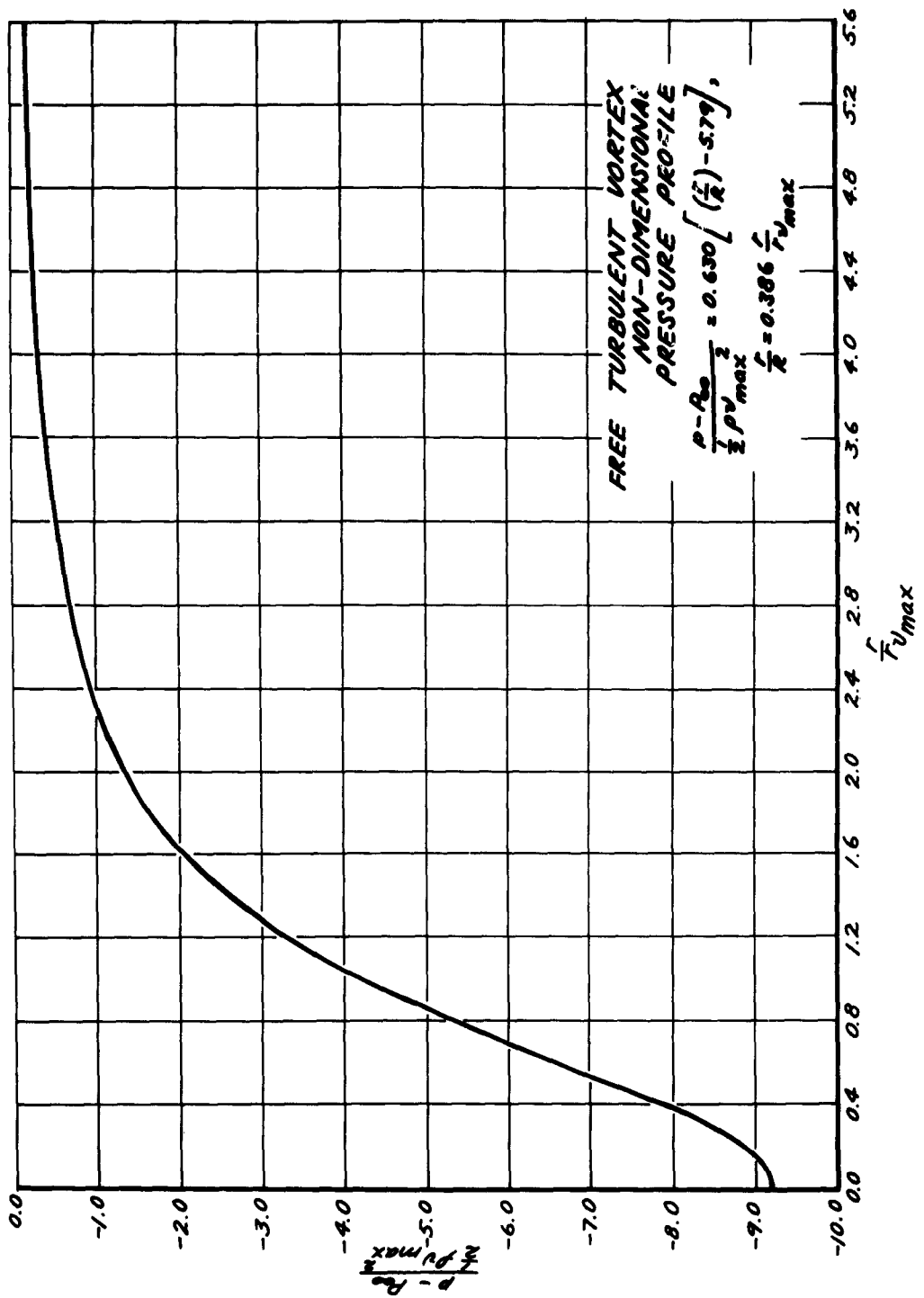FREE TURBULENT VORTEX
TYPICAL VARIATION OF RADIAL
VELOCITY PROFILES IN THE
AXIAL DIRECTION

$$u = -\frac{2.26\sqrt{K}}{R}\frac{dR}{dz}\frac{1}{\left(\frac{r}{R}\right)}\left[\left(\frac{r}{R}\right)^2(1+\beta_{30}) - \frac{1}{4}\left(\frac{r}{R}\right)^2 + \frac{1}{4\pi}\sin\pi\left(1-\frac{r}{R}\right)^2 - \frac{1}{2}T + 0.187\right]$$

POTENTIAL VORTEX
PROFILE

$z=1.5$ (EDGE OF BOUNDARY)
LAYER, $r = R$

OUTFLOW

INFLOW

u

r

$z=1.5$

$z=2$

$z=3$

$z=4$

$z=6$

$z=8$

$z=10$

$z_{1.5}$

z_2

z_3

z_4

z_6

z_8

z_{10}

SCHEMATIC DRAWING
OF VORTEX

Figure 14

FREE TURBULENT VORTEX
NON-DIMENSIONAL TANGENTIAL
VELOCITY PROFILE

$\frac{v}{v_{max}} = -0.561 \frac{R_{30}}{\left(\frac{r}{R}\right)} \left(\frac{r}{R}\right)$, $\frac{r}{R} = 0.386 \frac{r}{r_{v_{max}}}$

Figure 15

FREE TURBULENT VORTEX
NON-DIMENSIONAL
PRESSURE PROFILE

$$\frac{p - p_\infty}{\frac{1}{2}\rho v^2_{max}} = 0.630 \left[\left(\frac{r}{R}\right) - 5.79 \right],$$

$$\frac{r}{R} = 0.386 \frac{r}{r_{u_{max}}}$$

Figure 16

FREE TURBULENT VORTEX
NON-DIMENSIONAL AXIAL
VELOCITY PROFILE

$\frac{w}{W} = 1 + \beta_{3D}$, $\frac{r}{R} = 0.292$ $r\frac{w}{W} = 0.5$

Figure 17

Free Turbulent Vortex Non-Dimensional Radial Velocity Profile

Figure 18

Figure 19

COMPARISON OF THEORETICAL AND EXPERIMENTAL AXIAL VELOCITY DEFICIENCY IN A WING-TIP VORTEX

Figure 20

COMPARISON BETWEEN FREE VORTEX
THEORETICAL TANGENTIAL VELOCITY AND
CONFINED VORTEX EXPERIMENTAL
TANGENTIAL VELOCITY

○ EXPERIMENTAL POINTS,
13.5 INCHES FROM PLATE

— EQUATION 30

Figure 21A

CONFINED VORTEX EXPERIMENTAL
TANGENTIAL VELOCITY

1.5 INCHES FROM PLATE

Figure 21B

CONFINED VORTEX EXPERIMENTAL TANGENTIAL VELOCITY

5.5 INCHES FROM PLATE

r (FEET)

u (FPS)

Figure 21C

Figure 21D

CONFINED VORTEX EXPERIMENTAL TANGENTIAL VELOCITY

2.1.5 INCHES FROM PLATE

$$v = -\frac{\Gamma}{2\pi R}\frac{\beta_{3D}}{\left(\frac{r}{R}\right)} + kr$$

$\Gamma = 29.2$ FT.^{2}/SEC.
$k = 80.8$ SEC.$^{-1}$
$R = 0.0688$ FT.

Figure 21E

CONFINED VORTEX EXPERIMENTAL TANGENTIAL VELOCITY

26.5 INCHES FROM PLATE

$$v = -\frac{\Gamma}{2\pi R}\left(\frac{e^{\frac{kr^2}{r}}}{r}\right) + kr$$

$\Gamma = 26.3 \ FT.^2/SEC.$
$k = 104 \ SEC^{-1}$
$R = 0.0628 \ FT.$

Figure 22A

CONFINED VORTEX EXPERIMENTAL AXIAL VELOCITY

1.5 INCHES FROM PLATE
VELOCITY POSITIVE TOWARD THE PLATE

w (FPS)

r (FEET)

Figure 22B

Figure 22C

CONFINED VORTEX EXPERIMENTAL AXIAL VELOCITY

13.5 INCHES FROM PLATE

Figure 22D

CONFINED VORTEX EXPERIMENTAL AXIAL VELOCITY

21.5 INCHES FROM PLATE

w (FPS)

r (FEET)

Figure 22E

Figure 23

SCALE
DRAWING
OF
CONFINED
VORTEX
AXIAL
VELOCITY

26.5"

21.5"

SMOKE

13.5"

5.5"

1.5"

PLATE

Figure 24

CONFINED VORTEX EXPERIMENTAL
TANGENTIAL VELOCITY AT THREE
VARIAC SETTINGS

Figure 25

CONFINED VORTEX EXPERIMENTAL AXIAL VELOCITY AT THREE VARIAC SETTINGS